Journal of Alloys and Compounds 644 (2015) 763–769

Contents lists available at ScienceDirect

Journal of Alloys and Compounds

journal homepage: www.elsevier.com/locate/jalcom

Novel magnetic–dielectric composite ceramic obtained from $Y_3Fe_5O_{12}$ and $CaTiO_3$

D.V.M. Paiva [a], M.A.S. Silva [b], T.S. Ribeiro [c], I.F. Vasconcelos [c], A.S.B. Sombra [b], J.C. Góes [b], P.B.A. Fechine [a,*]

[a] Grupo de Química de Materiais Avançados (GQMAT), Departamento de Química Analítica e Físico-Química, Universidade Federal do Ceará – UFC, Campus do Pici, CP 12100, CEP 60451-970 Fortaleza, CE, Brazil
[b] Laboratório de Telecomunicações e Ciência e Engenharia de Materiais (LOCEM), Departamento de Física, Universidade Federal do Ceará, Brazil
[c] Laboratório de Magnetismo e Materiais Magnéticos, Departamento de Engenharia Metalúrgica e de Materiais, UFC, Brazil

ARTICLE INFO

Article history:
Received 12 February 2015
Received in revised form 6 May 2015
Accepted 8 May 2015
Available online 14 May 2015

Keywords:
YIG
CTO
Composite
Dielectric–magnetic materials

ABSTRACT

This work investigates the microstructure and magnetic–dielectric properties of the $CaTiO_3$ (CTO) and $Y_3Fe_5O_{12}$ (YIG) composite ceramic. CTO is a paramagnetic ceramic, presents a positive value of Resonant Frequency Temperature Coefficients (τ_f) and has high dielectric permittivity (ε_r) while YIG is ferromagnetic, has low ε_r and negative τ_f values. Therefore, it is expected that the composite from these individual phase shows new properties, or a mix of them derived from each component. X-ray powder diffraction (XRPD), Scanning Electron Microscope (SEM), Raman and ^{57}Fe Mössbauer spectroscopy were performed to confirm the phases of the composites. The dielectric and magnetic properties in Radio-Microwave frequencies were studied by impedance spectroscopy using different geometries. It was observed a densification improvement resulting from the insertion of the CTO in composites and a chemical reaction between YIG and CTO phases. This new composite has potential applications in bulk and thick/thin films devices.

1. Introduction

Recently, there has been a considerable upsurge in the study of ceramic materials due to their potentially useful for a wide variety of different applications such as sensors, biomaterials, fuel cells and electronic devices [1–3]. Here we can also highlight the telecommunication devices, which can be designed into a wide range of applications, including satellite communication systems, base stations and antennas. Some of them operating in the microwave region and ceramic materials present better properties than conventional materials. However, the materials appropriate for this use should present small size and higher efficiency (transmission, energetic etc.). In this miniaturization process, the material must present higher dielectric permittivity (ε_r) (antenna, for example) and higher thermal stability [4–6]. Due to this, composite ceramic materials have been appearing as promising alternative, where the mixture of distinct properties that are not interesting in the first moment, could result in another one (sum of the isolated phases) that can be applied [7–15].

Yttrium Iron Garnet ($Y_3Fe_5O_{12}$, YIG) is a traditional ceramic utilized in the microwave frequency system. It is an oxide commonly called ferrite, exhibit magnetic properties (ferrimagnetism) and dielectric properties ($\varepsilon_r = 16$ and dielectric loss tangent ($\tan\delta$) = 1×10^{-4}). However, this phase needs to be sintered at higher temperatures (~1500 °C). YIG also presents higher negative value (-283.82 ppm°C^{-1}) of the Resonant Frequency Temperature Coefficients (τ_f) and cubic symmetry with five iron site, two octahedral and three tetrahedral [16–22].

Calcium titanate ($CaTiO_3$, CTO) is an oxide from perovskite family and also one of most used in the microwave systems [23]. It has one of the highest ε_r value (160) for dielectric ceramics, allowing the miniaturization process of the electronic devices. It also presents low loss and a higher positive value of τ_f (850 ppm°C^{-1}) [23]. The crystalline structure of CTO presents an orthorhombic symmetry with paraelectric behavior [24–26].

Based on the above discussion, CTO and YIG phases were used in this present work to obtain the YIG_XCTO_{1-X} composite ceramics. It was the first time that these phases were used together and was expected that these materials working together to give the composite unique magnetic–dielectric features. Therefore, we reported the structure and morphology of the obtained material, furthermore the dielectric and magnetic properties measured in the Radio-Microwave frequencies. The production and study of the properties of this new composite are important due to their possible applications in bulk devices (microwave resonators, circulators

* Corresponding author.
E-mail address: fechine@ufc.br (P.B.A. Fechine).

http://dx.doi.org/10.1016/j.jallcom.2015.05.053
0925-8388/

and oscillators) and thick or thin films (Microstrip antennas) [16,22,27–30].

2. Experimental methods

2.1. Materials

The reagents utilized in this work were commercial products with analytical grade without further purification: calcium titanate ($CaTiO_3$ – 99.99%, Aldrich), iron oxide (Fe_2O_3 – 99.99%, Aldrich) and yttrium oxide (Y_2O_3 – (99.99%, Aldrich). $Y_3Fe_5O_{12}$ ceramic powder was synthesized according to the literature procedure [31]. Briefly, stoichiometric amounts of the starting materials (Fe_2O_3 and Y_2O_3) were milled for 1 h on a Fritsch Pulverisette 6 planetary mill in sealed stainless-steel vials under air. This step was used to give a good homogeneity and active the powder. After this, the powder was calcinated in air at 1150 °C for 5 h.

YIG and CTO were used to prepare the YIG_XCTO_{1-X} composite, where X (1, 0.75, 0.5, 0.25 and 0) was given in mass fraction (%). It was added PVA (5 wt.%) aqueous solution and this mixture was uniaxially pressed into pellets in a steel die. Final sintering was carried out at 1200 °C for 5 h (2 °C/min) in air.

2.2. Composites characterization

2.2.1. X-ray powder diffraction (XRPD)

The diffractograms were collected at room temperature (~300 K) from macerated samples of YIG, CTO, $YIG_{0.75}CTO_{0.25}$, $YIG_{0.50}CTO_{0.50}$ and $YIG_{0.25}CTO_{0.75}$. The equipment used was a PANalytical diffractometer (Xpert Pro MPD) operating at 40 kV and 45 mA in the geometry of Bragg–Brentano, with a Cu tube ($K\alpha_1$ = 1.540562 Å, $K\alpha_2$ = 1.54439 Å). To perform the analysis, the diffraction patterns were obtained in a range from 10° to 100° (2θ), with step of 0.013°. The analysis time at each step was 70 s in a graphite monochromator in the plane geometry for diffracted beam. The database ICSD (Inorganic Crystal Structure Database) was used to compare the diffraction patterns obtained from analysis and identify possible phases. The experimental patterns were numerically fitted with the Rietveld algorithm in a procedure to better identify and quantify crystallographic phases. The refined parameters were scale factor, phase fractions, background, cell dimensions, U and X parameters, and atomic coordinate parameters.

2.2.2. Raman spectroscopy

Retro micro-Raman system was used to obtain spectra of Raman scattering geometry. The excitation source used in the measurements was a He–Ne laser brand WITEC UHTS on line 300 emitting 633 nm. A triple spectrometer Jobin–Yvon T 64000 model was also used a CCD detector (Charge-Coupled Device) cooled to liquid nitrogen, a video camera coupled to a monitor and a microscope Olympus brand. The slits were adjusted to obtain a resolution of approximately 2 cm^{-1}.

2.2.3. ^{57}Fe Mössbauer spectroscopy

Mössbauer spectra of the samples containing iron were obtained using the spectrometer of FAST mark (Contec) Mössbauer Systems in transmission geometry. The measurements were performed at room temperature (~300 K), with 0.02 kg m^{-2} powdered sample. The radioactive source used in the analysis was ^{57}Co in rhodium matrix. The NORMOS software was used for fitting the Fe site in YIG for determination of the hyperfine parameters provides in the ^{57}Fe Mössbauer spectrum.

2.2.4. Scanning electron microscope

The surface's microstructure of the samples were obtained by Analytical Center of the Federal University of Ceará (UFC) using a scanning electron microscope Phillips XL-30, operating with a group of primary electrons with energy ranging from 12 to 20 keV. Rectangular samples of freeze-dried were covered with a carbon layer of about 30 nm thick.

2.2.5. Magneto-dielectric measurements

The magneto-dielectric properties of the YIG_XCTO_{1-X} composites were obtained by impedance spectroscopy (IS) at the radiofrequency. The data were collected in the frequency range of the 100 Hz–10 MHz and the Impedance Analyzer of Agilent Model 4294A was utilized. All measurements were performed at room temperature (300 K). For magnetic measurements, the experiments were performed using the Impedance Analyzer of Agilent E4991A model and an accessory Magnetic Material Text Fixture-Agilent 16454A in toroid shape samples. The toroid was fabricated in similar experimental procedure of ceramic pellets, i.e., the required amount was weighed and mixed with PVA, after sintered in the 1200 °C for 5 h (2 °C/min). The dimensions of the ceramics utilized are described in Table 1. The analyzed parameters were dielectric permittivity (ε_r), dielectric loss tangent ($\tan\delta$), magnetic permeability (μ_r) and magnetic loss tangent ($\tan\delta_M$).

Table 1
Dimensions of the toroids and pellets.

Sample	Toroids (mm)			Pellets (mm)	
	H	$Ø_{Outer}$	$Ø_{Inner}$	H	$Ø$
YIG	2.068	17.664	7.70	1.381	17.579
$YIG_{0.75}CTO_{0.25}$	2.202	17.377	7.55	1.509	17.332
$YIG_{0.50}CTO_{0.50}$	2.294	16.593	7.20	1.511	16.687
$YIG_{0.25}CTO_{0.75}$	2.485	15.695	6.80	1.609	15.564
CTO	–	–	–	1.563	14.677

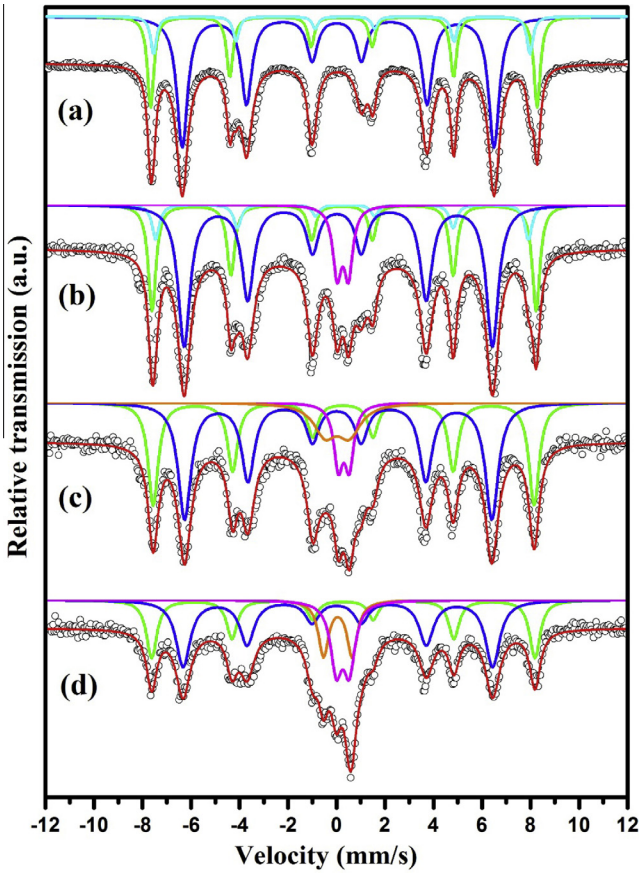

Fig. 1. Mössbauer spectra of the YIG_XCTO_{1-X} composites: (a) YIG, (b) $YIG_{0.75}CTO_{0.25}$, (c) $YIG_{0.50}CTO_{0.50}$ and (d) $YIG_{0.25}CTO_{0.75}$.

Table 2
Hyperfine parameters of the YIG_XCTO_{1-X} composites.

Sample	Sites	Hyperfine parameters			P (%)	Fe_{octa}/Fe_{tetra}
		δ (mms/s)	Δ (mm/s)	B_{HF} (T)		
YIG	16(a_1)	0.368149	0.0904016	49.4071	26.419	0.54
	4(a_2)	0.392577	−0.131645	48.1185	10.037	
	24(d)	0.1488115	0.0544059	39.8547	63.543	
$YIG_{0.75}CTO_{0.25}$	16(a_1)	0.381353	0.0847714	49.1117	25.535	0.62
	4(a_2)	0.398129	−0.109130	47.7013	8.373	
	24(d)	0.1528102	0.0615860	39.4120	54.945	
	O	0.3666	0.4641	–	11.147	–
$YIG_{0.50}CTO_{0.50}$	16(a_1)	0.388858	0.0304836	48.7003	32.928	1.24
	24(d)	0.1527935	0.0543175	39.2793	47.439	
	O	0.410084	0.450093	–	8.699	0.80
	T	0.1407560	0.997347	–	10.933	
$YIG_{0.25}CTO_{0.75}$	16(a_1)	0.381772	0.0151335	48.9986	27.566	0.65
	24(d)	0.1413685	0.0491824	39.5668	42.701	
	T	0.1634987	1.17799	–	12.774	1.33
	O	0.368129	0.534540	–	16.959	

Parameters: δ (isomer shifts): Δ (quadrupole splitting): B_{HF} (magnetic hyperfine field): P (iron ratio percentage error ~3%).

3. Results and discussion

The analysis from ^{57}Fe Mössbauer spectroscopy were required for verify the iron sites in the spectrum of YIG into the composites, as are shown in Fig. 1(a)–(d). For YIG sample (Fig. 1(a)), we can see the measured spectra (hollow black circles) with their respective fits (thick color solid curves): one sextet (green[1] curve) accounts for Fe^{3+} ions at sites with octahedral symmetry 16(a_1), whereas the other one (blue curve) corresponds to Fe^{3+} at tetrahedral coordinated sites 24(d). Thus, these two sextets are an indicative of the YIG phase [19,32,33] and they are present in all composites ($YIG_{0.75}CTO_{0.25}$, $YIG_{0.50}CTO_{0.50}$ and $YIG_{0.25}CTO_{0.75}$, Fig. 1(b)–(d), respectively). The third sextet (cyan curve) is associated to Fe^{3+} octahedral from site 4a_2 and is also characteristic for YIG. The hyperfine parameters obtained by fitting with three sites are according to that founded in the literature [18], as are shown in Table 2. The Fe_{octa}/Fe_{tetra} ratio was consistent with in the literature, i.e., 1:2.

It was also observed a paramagnetic phase (doublet pink curve) after addition of CTO in the composites and this phase concentration was increased as a function of quantity of the CTO. This paramagnetic phase was due to a new phase originated from a chemical reaction during the sinterization process between CTO and YIG. The probable phase originated of this reaction was $CaTi_{0.6}Fe_{0.4}O_{2.8}$ (CTFO). This may have happened due to the ion exchange of Ti^{4+} by Fe^{3+} which modify the local symmetry of the iron site in the YIG structure [34]. This was confirmed by fitting of Mössbauer spectra, in which the values of the quadrupole splitting for octahedral and tetrahedral sites was modify with the increasing of CTO phase in the composite. The adjusted hyperfine parameter for this paramagnetic phase was consistent with the hyperfine parameters for CFTO (Table 2).

The analysis of the Fe_{octa}/Fe_{tetra} ratio showed the preferential substitution of the iron by titanium in the YIG structure for $YIG_{0.75}CTO_{0.25}$ (0.62) and $YIG_{0.50}CTO_{0.50}$ (1.24) in the tetrahedral sites. The adjustment also shows that lost Fe_{tetra} in the YIG structure was incorporate in the CTO structure. The Grenier's work [34] showed the preferential incorporation of Ti^{4+} ions in tetrahedral site in the structure of the $CaFe_2O_4$. The ratio Fe_{octa}/Fe_{tetra} found adjustment in the CTFO spectra and it differs of the founded by Grenier. Thus, this can be explained by lability of the Fe^{3+} ions occupy both octahedral and tetrahedral sites and this ratio is affected by synthetic route.

XRPD was used to identify the crystalline structures present in the composites after sinterization process. Fig. 2 shows the XRPD patterns of the samples YIG_XCTO_{1-X} (X = 1, 0.75, 0.50, 0.25 and 0) and ICSD database patterns of CTO (ICSD: 74212) and YIG (ICSD: 23855) with the Rietveld refinements. For this purpose, the software DBWS Tools [35] was used to confirm the suggested structure and quantify the phases by Rietveld method's [36].

In Fig. 2, the green lines is the difference between the experimental (black dots – I_{Exp}) and the calculated (red line – I_{Calc}) intensity obtained from the refinement. Analyzing the general parameters for refinement, Rwp (weighted residual error) and S (quality factor "goodness of fit"), we can observe that refinement had acceptable values (Table 3), as seen in the literature [37] [38]. Although the R_{wp} and S demonstrate a good refinement, the R_{Bragg} showed values a little higher limit in literature and the mass fraction different from of the added in the composite (theoretical mass fraction). The R_{Bragg} is a parameter associated with structure of the crystalline phase utilized and when its value increase, could be that an inadequate structure was utilized. However, the R_{Bragg} values found here (between 4% and 16%) were not higher.

[1] For interpretation of color in Figs. 1 and 2, the reader is referred to the web version of this article.

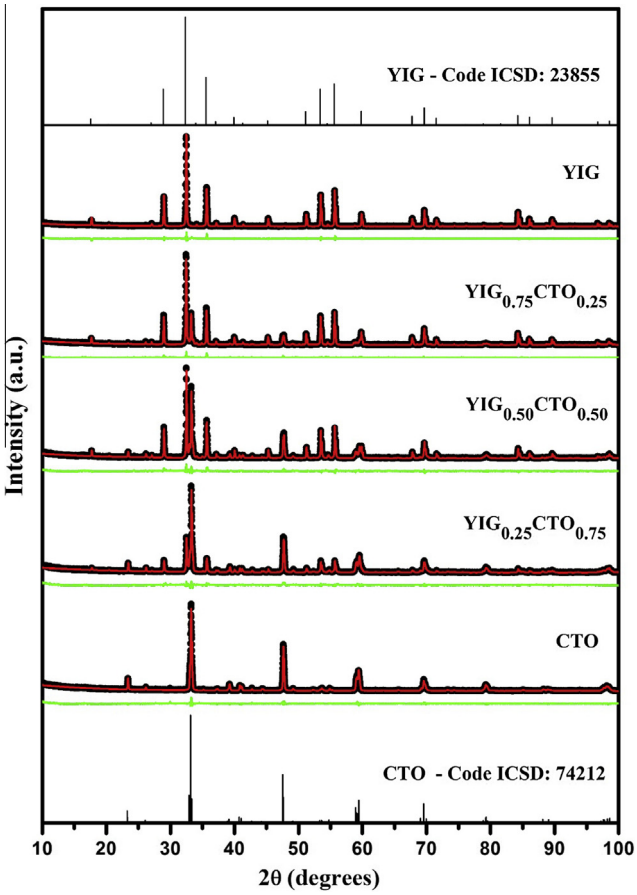

Fig. 2. Rietveld refinement of the X-ray diffraction pattern of YIG_XCTO_{1-X} composite powder. Additionally, the diffraction peaks of the YIG (database code ICSD 23855) and CTO (database code ICSD 74212) were used for identification and comparison.

The ^{57}Fe Mössbauer results helped to identify the CTFO phase beyond CTO and YIG in the composite. Due to this, Rietveld refinement was performed using CTFO phase. The insertion of this phase improved the refinement parameters. Table 3 presents the identified phases and their respective concentrations, crystallite size, density and their respective lattice parameters obtained by Rietveld refinement. The nominal and calculated values showed must consistent with insertion of third phase (CTFO). These values are different due to the CTFO phase in the $YIG_{0.75}CTO_{0.25}$, $YIG_{0.50}CTO_{0.50}$ and $YIG_{0.25}CTO_{0.75}$ composites. It was not possible demonstrate the insertion of the Ti^{4+} ions in the YIG crystal lattice, due to the non-existence of a crystallographic pattern in the ICSD. This can be observed in the R_{Bragg} for YIG phase, that increasing with CTO concentration, demonstrating that this diffraction patterns is not ideal for refinement. However, this did not invalidate the refinement performed.

The vibrational modes of an oxide can provide information on its crystal structure, which can be correlated with proposed structures by XRPD. From the analysis of the space group of the crystal, it was possible to predict how many vibrational modes are active in Raman spectroscopy [38]. Table 4 shows a comparative between the Raman modes obtained in this study with those reported in the literature [39–41]. For CTO structure, there are 24 Raman-active modes for orthorhombic structure with space group Pbnm (Z^B = 4) with four molecular units in three primitive cells, which can be described by the representation $\Gamma_{Raman,Pbnm} = 7A_g + 5B_{1g} + 7B_{2g} + 5B_{3g}$. The nine Raman modes (Table 4) observed in the range from 145 to 815 cm^{-1} are attributed to the orthorhombic

Table 3
Parameters obtained from Rietveld refinement of the YIG_XCTO_{1-X} composites.

Sample	Phase	Lattice parameters			R_{wp} (%)	R_{Bragg}	S	V_{cell}	Nominal (wt%)	Quantitative phase analysis (wt%)	Density (g/cm^{-3})	Crystallite size (nm)
		a (Å)	b (Å)	c (Å)								
YIG	YIG	12.3764	12.3764	12.3764	8.94	6.57	1.37	1895.76	100	100	5.173	91.3
$YIG_{0.75}CTO_{0.25}$	YIG	12.3779	12.3779	12.3779	9.16	7.31	1.39	1896.43	75	65.10	5.171	83.1
	CTFO	5.3598	5.4830	7.6348		9.66		224.37	–	18.33	4.034	56.1
	CTO	5.3780	5.4420	7.6400		15.67		223.60	25	16.57	4.041	35.6
$YIG_{0.50}CTO_{0.50}$	YIG	12.3769	12.3769	12.3769	9.80	10.32	1.42	1895.96	50	42.57	5.172	96.4
	CTFO	5.3635	5.4737	7.6371		5.70		224.21	–	17.72	4.037	40.7
	CTO	5.3754	5.4525	7.6399		5.74		223.92	50	39.57	4.035	64.8
$YIG_{0.25}CTO_{0.75}$	YIG	12.3762	12.3762	12.3762	12.19	14.47	1.56	1895.68	25	19.91	5.173	77.7
	CTFO	5.3709	5.4609	7.6399		9.76		224.08		17.21	4.040	69.4
	CTO	5.3794	5.4459	7.6437		7.67		223.93	75	62.88	4.035	56.9
CTO	CTO	5.3848	5.4358	7.6428	12.01	4.89	1.32	223.71	100	100	4.039	53.2

Table 4
Raman shift (in cm^{-1}) of the YIG_XCTO_{1-X} composites.

YIG Assignments		$YIG_{0.75}$ $CTO_{0.25}$	$YIG_{0.50}$ $CTO_{0.50}$	$YIG_{0.25}$ $CTO_{0.75}$	CTO Assignments	
$T + T_1 + T_2$	118	121	118	114	–	–
–	–	–	–	147	149	Lattice mode Ca–TiO_3
$T + T_1 + T_2$	163	163	163	–	–	–
–	–	–	–	173	174	δ_{O-Ti-O}
$T + T_1 + T_2$	183	184	183	–	–	–
–	–	221	220	219	219	δ_{O-Ti-O}
$L[FeO_4]^{5-}$	228	–	–	–	–	–
–	–	–	243	241	241	δ_{O-Ti-O}
$L[FeO_4]^{5-}$	263	264	264	264	–	–
–	–	286	286	284	285	δ_{O-Ti-O}
–	–	–	–	333	332	δ_{O-Ti-O}
$\nu_4(F_{2g})$	338	338	338	–	–	–
$\nu_4(F_{2g})$	370	371	371	–	–	–
$\nu_4(F_{2g})$	–	–	–	379	–	–
$\nu_2(E_g)$	412	412	412	–	–	–
$\nu_2(E_g)$	441	441	443	–	–	–
–	–	469	472	471	470	τ_{Ti-O3}
–	–	–	497	492	495	τ_{Ti-O3}
$\nu_2(A_{1g})$	502	501	–	–	–	–
$\nu_3(F_{2g})$	586	587	585	–	–	–
$\nu_3(E_g)$	623	–	624	624	–	–
–	–	–	–	–	644	υ_{Ti-O}
$\nu_3(F_{2g})$	678	678	676	–	–	–
$\nu_3(F_{2g})$	–	–	–	683	–	–
$\nu_1(A_{1g})$	–	–	–	714	–	–
$\nu_1(A_{1g})$	736	738	737	–	–	–

structure, in agreement with the literature [40]. Fig. 3 shows the spectrum of the CTO with its main modes.

For YIG phase (Fig. 3), the analysis of the cubic structure with space group Ia3d predicts 25 Raman-active modes which can be represented by the description: $\Gamma_{Raman,Ia3d} = 3A_{1g} + 8E_g + 14F_{2g}$. However, the Raman spectrum presented 14 internal modes of the FeO_4 group ($2\upsilon_1$, $4\upsilon_2$, $4\upsilon_3$ and $4\upsilon_4$) [39]. These modes are associated with internal vibrations of the FeO_4 molecular group, whereas the modes under 300 cm^{-1} were labeled as translations (T) of Y^{3+}, $[FeO_4]^{5-}$. Raman spectra of the YIG_XCTO_{1-X} showed enough similarity with the isolated phases. The range of 100–500 cm^{-1} was the region where the greatest amount of vibrational modes of the material involved appears. The lack of other bands reinforces the discussion about isomorphic phases from reaction between YIG and CTO.

The morphology of the composites (surface, porosity and densification) was investigated by Scanning Electron Microscope (SEM). In Fig. 4, we present photomicrographs of the samples YIG (a), $YIG_{0.75}CTO_{0.25}$ (b), $YIG_{0.50}CTO_{0.50}$ (c) and CTO (d). For YIG sample (Fig. 4(a)), one can notice globular shapes with aggregated grains

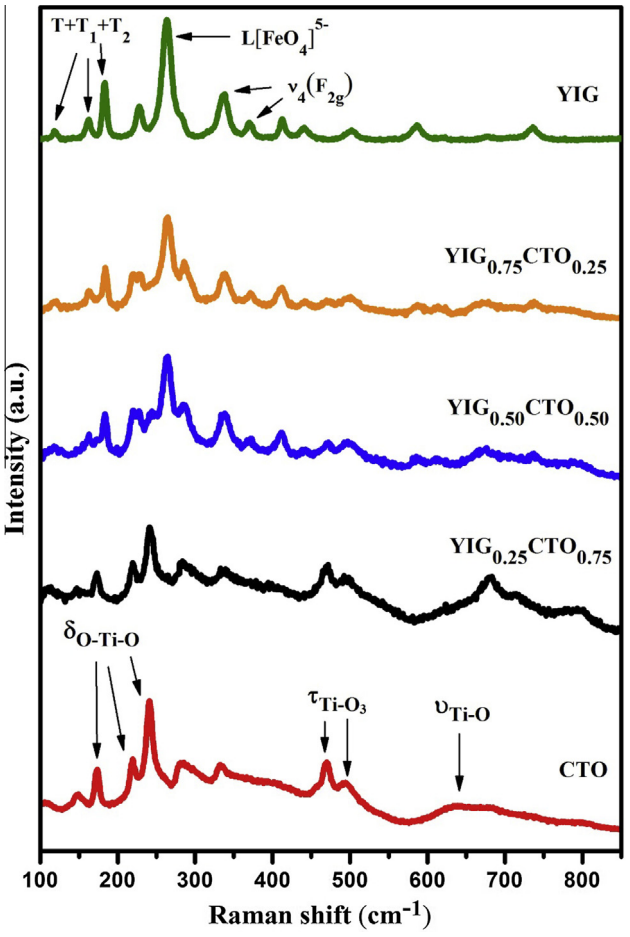

Fig. 3. Raman spectra of vibrational modes of the YIG_XCTO_{1-X} composites.

and low porosity. The addition of the CTO in the $YIG_{0.75}CTO_{0.25}$ (Fig. 4(b)) and $YIG_{0.50}CTO_{0.50}$ (Fig. 4(c)) composites markedly enhance the densification of the material and promote grain growth. One can also notice a reasonable homogenization, due to good grain distribution. In the case of the CTO (Fig. 4(d)), we can observe a reasonable homogenization, due to good grain distribution. This sample showed the highest densification in comparison with the other ones.

The knowledge of dielectric behavior has great importance due to the several devices operating in different frequencies range. For instance, in the radiofrequency range, the main method used to

data acquisition is IS. In this sense, the dielectric properties were obtained by measuring of the capacitance (Cp) and dissipation factor (D), where the dielectric permittivity (ε_r) was calculated by Eq. (1) and the dielectric loss tangent ($\tan\delta$) is equal the D [38].

$$\varepsilon_r = \frac{Cp * h}{\varepsilon_0 * A} \quad (1)$$

where Cp is the capacitance of ceramic capacitor formed with sample (Farad); h is the height of pellet ceramic (m); A is the area of the pellet face (m^2) and ε_0 is vacuum permittivity (Farad m^{-1}).

Fig. 5 shows the dielectric behavior (ε_r and $\tan\delta$) of the composites samples. The dielectric spectrum showed an increase of the ε_r as a function of CTO concentration. This happened due to the CTO has higher ε_r values than YIG phase, for example, ε_r for CTO at 100 Hz was 238.4, while YIG presented 55.3. It was also observed that composites presented ε_r values approximately constants in the analyzed frequency range. The exception was $YIG_{0.25}CTO_{0.75}$, which showed a decrease until 10 kHz. It was noted that the ε_r for all samples also had slightly lower values for higher frequencies. However, this behavior is already known for dielectric materials on the electric external field, and can be explained by dipole relaxation phenomenon [42]. This high ε_r values at low frequencies is associated with two types of polarization: space charge polarization due non-homogenization of the dielectric structure and the Maxwell–Wagner interfacial polarization type, which is in agreement with Koops phenomenological theory [43]. Fig. 5 also shows a decrease of the $\tan\delta$ values with increasing of CTO concentrations in the YIG_XCTO_{1-X} composites. Therefore, there was a modification of the dielectric properties (ε_r and $\tan\delta$) due to the mutual influence of both phases. CTO addition improved the $\tan\delta$ of the composites, for example, YIG and $YIG_{0.50}CTO_{0.50}$ had values of the 0.0147 and 0.00302 at 1 MHz, respectively. These values were lower than other composites studied in the literature, as YIG–GdIG [44], and more satisfactory for device application.

The classic treatment applied for two or more phases present in a dielectric (law of Lichtenecker and Claussius–Mosotti) [45] was used to estimate the ε_r behavior in composites. The dielectric mixture model proposed by Lichtenecker is an empirical logarithmic rule for the ε_r and the dielectric constants (ε_i) of the individual phases. It is given by $ln\varepsilon_r = \sum_i x_i ln\varepsilon_i$, where x_i is the percentage of weight in each component. Therefore, fractional mass (x_i) and ε_i of each constituent are the main parameters used in calculating the effective ε of the mixture. However, for Claussius–Mosotti law, the dielectric constant values are described by (2).

$$\frac{\varepsilon_{COMPOSITE} - 1}{\varepsilon_{COMPOSITE} + 2} = (1 - x)\frac{\varepsilon_{YIG} - 1}{\varepsilon_{YIG} + 2} + x\frac{\varepsilon_{CTO} - 1}{\varepsilon_{CTO} + 1} \quad (2)$$

Fig. 6 shows the profile of ε_r values of the YIG_XCTO_{1-X} composites measured at 100 kHz as a function of CTO mass fraction (%) and the plot of Lichtenecker and Claussius–Mosotti mixture laws. The experimental ε_r values are in better agreement with the calculated by Lichtenecker (black lines). However, one physical parameter which influences the ε_r value is the relative density, where values below unit showed ε_r lowest than the expected for a dense ceramic. This can be explained by pores in the ceramic that presented, in general, ε_r lowest than a dense ceramic. Thus, the Claussius–Mosotti rule was used by corrections of permittivity without

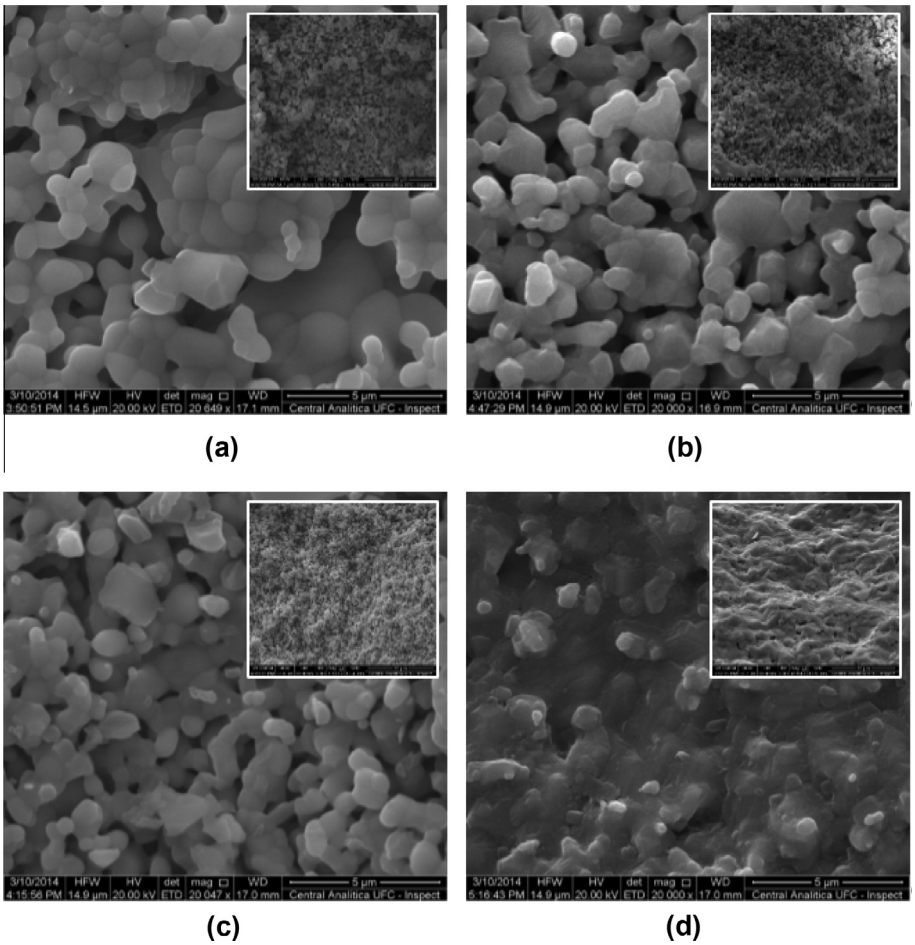

Fig. 4. Scanning electron photomicrograph (SE) of YIG (a), $YIG_{0.75}CTO_{0.25}$ (b), $YIG_{0.50}CTO_{0.50}$ (c) and CTO (d) at an amplification of 20,000× and 5000× (inset).

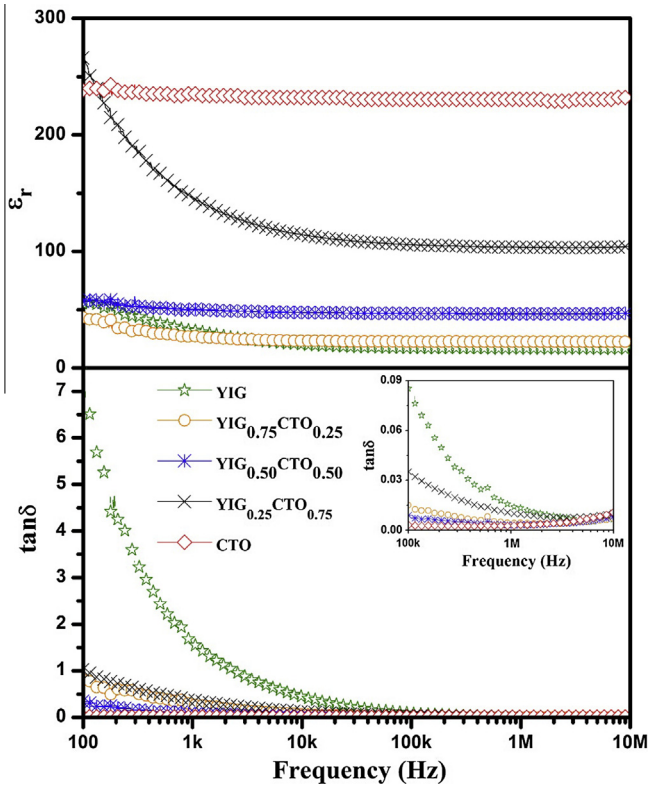

Fig. 5. Dielectric measurements of YIG_XCTO_{1-X} composites in the radiofrequency range.

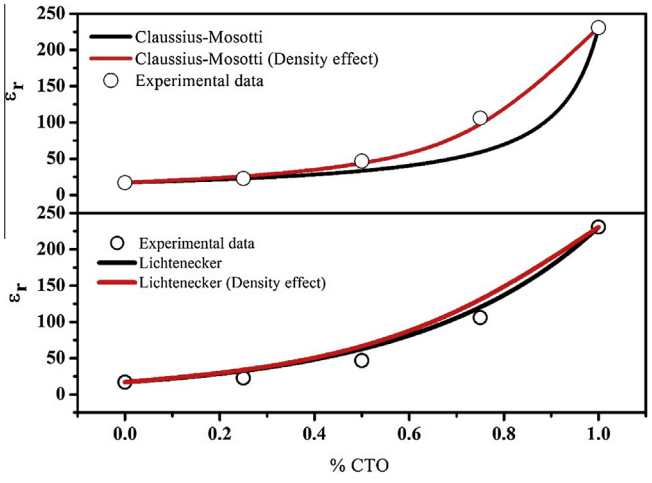

Fig. 6. Dielectric properties in the 100 kHz for YIG_XCTO_{1-X} compared with Lichtenecker and Claussius–Mosotti mixture rules.

porosity, the relative density obtained was 0.61 (YIG), 0.662 ($YIG_{0.75}CTO_{0.25}$), 0.75 $YIG_{0.75}CTO_{0.25}$, 0.866 ($YIG_{0.75}CTO_{0.25}$) and 0.937 (CTO). One can observe that Claussius–Mosotti rule demonstrated the best correlation with experimental, as shown in Fig. 6.

Fig. 7 shows magnetic measurement (μ_r and $\tan\delta_M$) in the frequency range from 50 MHz to 1.5 GHz. It was expected a decreasing of the magnetic permeability (μ_r) with increasing the CTO concentration. However, this behavior was observed only in the frequencies before 500 MHz. The μ_r values of the composites were higher than YIG ceramic after this frequency, as we can see in Fig. 7 and Table 4. This result suggested that another phase (CTFO) changed the magnetic properties of the composites, increasing the μ_r at

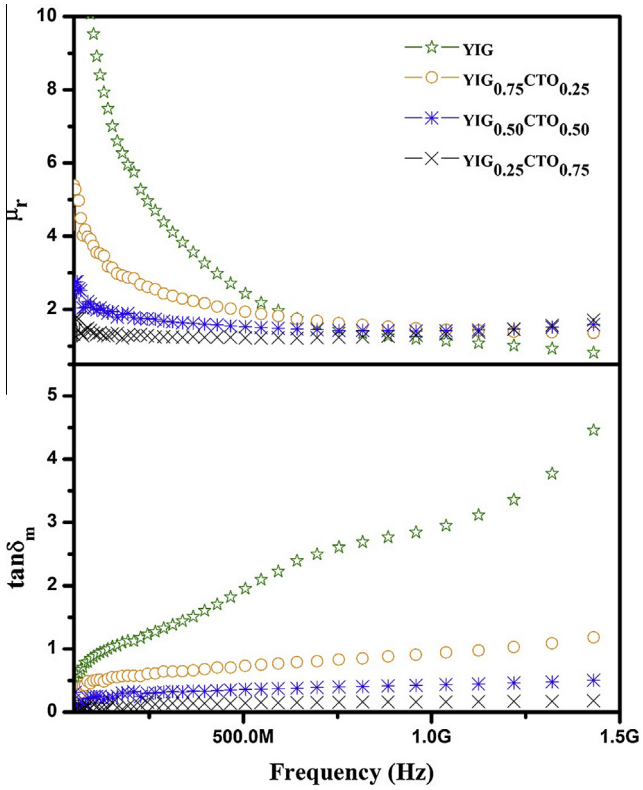

Fig. 7. Magnetic measurements of YIG_XCTO_{1-X} composite: μ_r and $\tan\delta_M$.

Table 5
Dielectric properties in radiofrequency range for YIG_XCTO_{1-X} composites.

Sample	100 MHz		500 MHz		1 GHz		1.5 GHz	
	μ_r	tan μ	μ_r	tan μ	μ_r	tan μ	μ_r	tan μ
YIG	9.59	0.877	2.47	1.94	1.17	2.912	0.75	5.069
$YIG_{0.75}CTO_{0.25}$	3.77	0.478	1.95	0.729	1.47	0.925	1.36	1.249
$YIG_{0.50}CTO_{0.50}$	2.1	0.204	1.53	0.356	1.42	0.431	1.66	0.523
$YIG_{0.25}CTO_{0.75}$	1.39	0.0893	1.22	0.146	1.32	0.167	1.85	0.183

higher frequencies, as is shown in Table 5. The change of the Fe^{3+} by Ti^{4+}in the YIG structure, might have promote the increasing in the magnetic permeability of the composite.

4. Conclusion

YIG_XCTO_{1-X} composites were characterized by XRPD, Raman and Mössbauer spectroscopy. The density of composites was improved with addition of CTO. Furthermore, it was confirmed the formation of an intermediate phase, isostructural of CTO (CTFO), originated from ion exchange of the Fe^{3+} (YIG) by Ti^{4+} (CTO). This phase was formed by reaction between YIG and CTO. However, CFTO was important to improve the dielectric and magnetic properties of the composites. Our results indicate that this composite has potential application for miniaturization device process due to the ε_r and μ_r values. It could be also applied as a dielectric-ferromagnetic resonator antenna and filter owing to the dielectric and magnetic properties.

Acknowledgments

We gratefully acknowledge the financial support of Brazilian Agencies for Scientific and Technological Development CAPES,

Funcap, Central Analitica UFC/CT-INFRA/MCTI-SISNANO/Pró-Equipamentos CAPES and CNPq.

References

[1] E.J.J. Mallmann, J.C. Góes, S.D. Figueiró, N.M.P.S. Ricardo, J.C. Denardin, A.S.B. Sombra, F.J.N. Maia, S.E. Mazzeto, P.B.A. Fechine, Microstructure and magneto-dielectric properties of the chitosan/gelatin-YIG biocomposites, Express Polym. Lett. 5 (2011) 1041–1049.

[2] N.D.G. Souza, R.M. Freire, A.P. Cunha, M.A.S. da Silva, S.E. Mazzetto, A.S.B. Sombra, J.C. Denardin, N.M.P.S. Ricardo, P.B.A. Fechine, New magnetic nanobiocomposite based in galactomannan/glycerol and superparamagnetic nanoparticles, Mater. Chem. Phys. 156 (2015) 113–120.

[3] T.C.S. of Japan, Advanced Ceramic Technologies & Products, Springer, 2012.

[4] D. Kajfez, P. Guillon, Dielectric Resonators, Noble Publishing Corporation, 1998. p. 547.

[5] A. Petosa, Dielectric Resonator Antenna Handbook, Artech House, 2007. p. 308.

[6] K.M. Luk, K.W. Leung, Dielectric Resonator Antennas, Research Studies Press, 2003. p. 388.

[7] M. Teirikangas, J. Juuti, H. Jantunen, Layered dielectric–magnetic composite structures for Rf-applications, Compos. Struct. 93 (1) (2010) 179–183.

[8] H.H.B. Rocha, F.N.A. Freire, R.R. Silva, D.X. Gouveia, J.M. Sasaki, M.R.P. Santos, J.C. Góes, A.S.B. Sombra, Structural properties study of the magneto-dielectric composite: $Cr_{0.75}Fe_{1.25}O_3$ (CRFO):$Fe_{0.5}Cu_{0.75}Ti_{0.75}O_3$ (FCTO), J. Alloys Comp. 481 (2009) 438–445.

[9] A. Manuel Stephan, K.S. Nahm, Review on composite polymer electrolytes for lithium batteries, Polymer (Guildf) 47 (16) (2006) 5952–5964.

[10] B. Kumar, L.G. Scanlon, Polymer–ceramic composite electrolytes: conductivity and thermal history effects, Solid State Ionics 124 (1999) 239–254.

[11] R. Jayakumar, D. Menon, K. Manzoor, S.V. Nair, H. Tamura, Biomedical applications of chitin and chitosan based nanomaterials – a short review, Carbohydr. Polym. 82 (2) (2010) 227–232.

[12] W.D. Callister, D.G. Rethwisch, Materials Science and Engineering: An Introduction, ninth ed., 2013, p. 992.

[13] P. Niemiec, D. Bochenek, A. Chrobak, P. Guzdek, A. Błachowski, Ferroelectric–ferromagnetic ceramic composites based on PZT with added ferrite, Int. J. Appl. Ceram. Technol. 12 (2015) E82–E89.

[14] J. Kulawik, D. Szwagierczak, P. Guzdek, Magnetic, magnetoelectric and dielectric behavior of $CoFe_2O_4$–$Pb(Fe_{1/2}Nb_{1/2})O_3$ particulate and layered composites, J. Magn. Magn. Mater. 324 (19) (2012) 3052–3057.

[15] P. Guzdek, M. Sikora, Góra, C. Kapusta, Magnetic and magnetoelectric properties of nickel ferrite-lead iron niobate relaxor composites, J. Eur. Ceram. Soc. 32 (2012) 2007–2011.

[16] P.B.A. Fechine, R.S.T. Moretzsohn, R.C.S. Costa, J. Derov, J.W. Stewart, A.J. Drehman, C. Junqueira, A.S.B. Sombra, Magneto-dielectric properties of the $Y_3Fe_5O_{12}$ and $Gd_3Fe_5O_{12}$ dielectric ferrite resonator antennas, Microw. Opt. Technol. Lett. 50 (11) (2008) 2852–2857.

[17] R.D. Sánchez, C.A. Ramos, J. Rivas, P. Vaqueiro, M.A. López-Quintela, Ferromagnetic resonance and magnetic properties of single-domain particles of $Y_3Fe_5O_{12}$ prepared by sol–gel method, Phys. B Condens. Matter 354 (1–4) (2004) 104–107.

[18] J.M. Greneche, H. Pascard, J.R. Regnard, Modification of [FeO_4] tetrahedral site number induced by fast-neutron irradiation in $Y_3Fe_5O_{12}$ investigated by Mössbauer spectroscopy, Solid State Commun. 65 (7) (1988) 713–717.

[19] E. Garskaite, K. Gibson, A. Leleckaite, J. Glaser, D. Niznansky, A. Kareiva, H.-J.J. Meyer, On the synthesis and characterization of iron-containing garnets ($Y_3Fe_5O_{12}$, YIG and $Fe_3Al_5O_{12}$, IAG), Chem. Phys. 323 (2–3) (2006) 204–210.

[20] S. Khanra, A. Bhaumik, Y.D. Kolekar, P. Kahol, K. Ghosh, Structural and magnetic studies of $Y_3Fe_{5-5x}Mo_{5x}O_{12}$, J. Magn. Magn. Mater. 369 (2014) 14–22.

[21] F.W. Aldbea, N.B. Ibrahim, M. Yahya, Effect of adding aluminum ion on the structural, optical, electrical and magnetic properties of terbium doped yttrium iron garnet nanoparticles films prepared by sol–gel method, Appl. Surf. Sci. 321 (2014) 150–157.

[22] C.-C. Huang, Y.-H. Hung, J.-Y. Huang, M.-F. Kuo, Performance improvement of S-band phase shifter using Al, Mn and Gd doped $Y_3Fe_5O_{12}$ and sintering optimization, J. Alloys Comp. (2014).

[23] M.T. Sebastian, Dielectric Materials for Wireless Communication, Elsevier Science, 2010. p. 688.

[24] A.D.S.B. Costa, M.C. Romeu, R.C.S. Costa, T.S.M. Fernandes, F.W.D.O. Amarante, M.A.S. Da Silva, G.D. Saraiva, A.S.B. Sombra, A.D.S. Bruno Costa, D.G. Sousa, High thermal stability of the microwave dielectric properties of $CaTi_{1-x}(Nb_{2/3}Li_{1/3})_xO_{3-\delta}$ alloys, J. Adv. Dielectr. 01 (5) (2011) 417–427. Nov. 2011.

[25] C.L. Huang, M.H. Weng, Improved high Q value of $MgTiO_3$–$CaTiO_3$ microwave dielectric ceramics at low sintering temperature, Mater. Res. Bull. 36 (2001) 2741–2750.

[26] H. Jantunen, R. Rautioaho, A. Uusimäki, S. Leppävuori, Compositions of $MgTiO_3$–$CaTiO_3$ ceramic with two borosilicate glasses for LTCC technology, J. Eur. Ceram. Soc. 20 (14–15) (2000) 2331–2336.

[27] B.D. Lee, H.R. Lee, K.H. Yoon, Y.S. Cho, Microwave dielectric properties of magnesium calcium titanate thin films, Ceram. Int. 31 (2005) 143–146.

[28] P.B.A. Fechine, A. Távora, L.C. Kretly, A.F.L. Almeida, M.R.P. Santos, F.N.A. Freire, A.S.B. Sombra, Microstrip antenna on a high dielectric constant substrate: $BaTiO_3$ (BTO)–$CaCu_3Ti_4O_{12}$ (CCTO) composite screen-printed thick films, J. Electron. Mater. 35 (2006) 1848–1856.

[29] A.F.L. Almeida, P.B.A. Fechine, L.C. Kretly, A.S.B. Sombra, $BaTiO_3$ (BTO)–$CaCu_3Ti_4O_{12}$ (CCTO) substrates for microwave devices and antennas, J. Mater. Sci. 41 (14) (2006) 4623–4631.

[30] G.N. Rocha, L.F.L. Melo, M.A.S. da Silva, P.V.S. Silva, A.S.B. Sombra, P.B.A. Fechine, Study of the performance of dielectric resonator antennas based on the matrix BiREWO6 [RE = Gd, Y, Nd], Microw. Opt. Technol. Lett. 54 (1) (2012) 18–23.

[31] P.B.A. Fechine, F.M.M. Pereira, M.R.P. Santos, F.P. Filho, A.S. de Menezes, R.S. de Oliveira, J.C. Góes, L.P. Cardoso, A.S.B. Sombra, Microstructure and magneto-dielectric properties of ferrimagnetic composite $GdIG_X$:YIG_{1-X} at radio and microwave frequencies, J. Phys. Chem. Solids 70 (5) (2009) 804–810.

[32] K. Nomura, T. Hanai, R. Sadamoto, Y. Ujihira, T. Ryuo, M. Tanno, Conversion electron Mössbauer spectroscopic study of YIG substituted with Bi, Ti, Ga and La, Hyperfine Interact. 84 (1) (1994) 421–426.

[33] H.M. Widatallah, C. Johnson, S.H. Al-Harthi, A.M. Gismelseed, A.D. Al-Rawas, S.J. Stewart, M.E. Elzain, I.A. Al-Omari, A.A. Yousif, A structural and Mössbauer study of $Y_3Fe_5O_{12}$ nanoparticles prepared with high energy ball milling and subsequent sintering, Hyperfine Interact. 183 (1–3) (2008) 87–92.

[34] J.-C. Grenier, F. Menil, M. Pouchard, P. Hagenmuller, Mössbauer resonance studies in the $CaTiO_3$–$Ca_2Fe_2O_5$ system, Mater. Res. Bull. 13 (2) (1978) 329–337.

[35] L. Bleicher, J.M. Sasaki, C.O. Paiva Santos, Development of a graphical interface for the Rietveld refinement program DBWS, J. Appl. Crystallogr. 33 (4) (2000) 1189.

[36] H.M. Rietveld, Line profiles of neutron powder-diffraction peaks for structure refinement, Acta Crystallogr. 22 (1) (1967) 151–152.

[37] C. Pascoal, R. Machado, V.C. Pandolfelli, Determinação de fase vítrea em bauxitas refratárias, Cerâmica 48 (306) (2002) 61–69.

[38] P.M.O. Silva, T.S.M. Fernandes, R.M.G. Oliveira, M.A.S. Silva, A.S.B. Sombra, Radiofrequency and microwave properties study of the electroceramic $BaBi_4Ti_4O_{15}$, Mater. Sci. Eng. B 182 (2014) 37–44.

[39] P.B.A. Fechine, E.N. Silva, A.S. de Menezes, J. Derov, J.W. Stewart, A.J. Drehman, I.F. Vasconcelos, A.P. Ayala, L.P. Cardoso, A.S.B. Sombra, Synthesis, structure and vibrational properties of $GdIG_X$:YIG_{1-X} ferrimagnetic ceramic composite, J. Phys. Chem. Solids 70 (1) (2009) 202–209.

[40] L.S. Cavalcante, V.S. Marques, J.C. Sczancoski, M.T. Escote, M.R. Joya, J.A. Varela, M.R.M.C. Santos, P.S. Pizani, E. Longo, Synthesis, structural refinement and optical behavior of $CaTiO_3$ powders: a comparative study of processing in different furnaces, Chem. Eng. J. 143 (1–3) (2008) 299–307.

[41] T.M. Mazzo, M.L. Moreira, I.M. Pinatti, F.C. Picon, E.R. Leite, I.L.V. Rosa, J.A. Varela, L.A. Perazolli, E. Longo, $CaTiO_3$:Eu^{3+} obtained by microwave assisted hydrothermal method: a photoluminescent approach, Opt. Mater. (Amst) 32 (9) (2010) 990–997.

[42] E. Barsoukov, J.R. Macdonald, Impedance Spectroscopy: Theory, Experiment, and Applications, Wiley, 2005.

[43] B. Raneesh, H. Soumya, J. Philip, S. Thomas, K. Nandakumar, Magnetoelectric properties of multiferroic composites $(1-x)ErMnO_{3-x}Y_3Fe_5O_{12}$ at room temperature, J. Alloys Comp. 611 (2014) 381–385.

[44] P.B.A.B.A. Fechine, F.M.M.M.M. Pereira, M.R.P.R.P. Santos, F.P.P. Filho, A.S.S. de Menezes, R.S.S. de Oliveira, J.C.C. Góes, L.P.P. Cardoso, A.S.B.S.B. Sombra, Microstructure and magneto-dielectric properties of ferrimagnetic composite $GdIG_X$:YIG_{1-X} at radio and microwave frequencies, J. Phys. Chem. Solids 70 (5) (2009) 804–810.

[45] A.J. Moulson, J.M. Herbert, Electroceramics: Materials, Properties, Applications, Wiley, 2003.